Characterization of structure and composition of quantum dots by transmission electron microscopy

K. Scheerschmidt and P. Werner

1 Introduction

Electron microscope techniques provide very powerful tools to investigate nanometer scaled structures in solids, especially by using high resolution electron microscopy (HREM) and conventional transmission electron microscopy (TEM). The present overview describes the possibilities of investigating quantum dot (QD) structures by TEM and HREM, discussing advantages and disadvantages, presuppositions needed, limitations, and the problems of contrast analysis and interpretation in comparison with other structure analyzing methods.

1.1 Quantum dots: structural properties

Quantum dots (QDs) are nanometer scaled regions of suitable material embedded in semiconductor or other matrices. The possibilities of arranging such QDs into complex arrays implies many opportunities for scientific investigations and technological application. There was a breakthrough, when it became possible to create high-density arrays of QDs by the epitaxial growth of lattice mismatched heterostructures (Stranski-Krastanow growth mode), such as vertically stacked InAs islands on a GaAs substrate. Concerning their technological application, QD structures are most attractive for active as well as passive optoelectronic devices (e.g., vertical cavity surface emitting lasers, VCSEL). However, depending on the growth techniques applied (mainly MBE and MOCVD), the islands differ in size, shape, chemical composition and lattice strain. Nanometer scaled confinement of electrons in quantum well and quantum dot structures influences and determines the optoelectronic device properties in an essential way. Especially shape, size and strain field of single QDs as well as the quality, density, and homogeneity of equisized and equishaped dot arrangements are important features of QDs which control the optical properties, the emission and absorption of light, the lasing efficiency, and other optoelectronic device properties [1,2]. Whether the QDs may be useful for future applications, for instance, as controlled-NOT for Qbits in quantum computing [3], depends also strongly on the structural properties. Since the first demonstration of photopumping [4] and injection lasing [5], the large number of QD investigations have given a certain insight into the

requirements for the structural properties to obtain a sufficiently sharp distribution of the electron density and strong confinement of wavefunctions (cf. [1–10] and the contributions in this volume). A critical minimum QD size is required to confine at least one electron/exciton in the dot. A critical maximum QD size is related to the critical separation of the energy levels for thermally induced decoupling. Uniformity of the QD size is necessary to ensure coupling of states between QDs. The localization of states and their stability depend further on composition and strain of the QDs. This is also important for the self-organized formation and lateral arrangement, vertical stacking on top or between buried dots, or preordering by surface structuring of QDs as, e.g., due to steps or mono-layer growth along vicinal surfaces (cf., e.g. [9,11,12]). Finally, an extension of the emission range towards longer wavelength needs better understanding and handling of controlled growth via lattice mismatched hetero-structures or self-assembling phenomena (see, e.g., [13]). As dealed with in the following the TEM techniques provide suitable tools to control the important QD parameters discussed here.

1.2 Quantum dots: structural investigations

A wide variety of imaging methods (scanning tunneling microscopy STM, atomic force microscopy AFM, scanning transmission electron microscopy STEM, energy filtered electron microscopy EFTEM, etc.) are used to investigate the growth, the self-assembling, and the physical properties of quantum dots. Among these the cross-section HREM and the plan-view TEM imaging techniques are suitable methods to characterize directly the shape, the size, and the strain field of nanometer scaled structures and related defects, especially using electron diffraction contrast imaging (DC) with bright field (BF) and dark field (DF) modes. Electron microscope imaging is the only direct method of structure investigation with a sufficient resolution for capped QDs without destroying the buried dots. Such a phenomenological TEM analysis may directly confirm whether dots have formed in the strain field of buried dots, the dot height may be proportional to the deposited material, QD dispersion varies with stacking number or is bimodal, strains variies with dot layer spacing, and QD composition is smooth or inhomogeneous, etc. (cf., e.g., applications in the systems GeSi [14–16], GeSiC [17], AlGaAs [18,19], InGaAs [20–23], SiInGaAs [24], InAsP [25], CdZnSe [26–28], InGaN [29,30], GaInP [31], $SiSiO_2$ [32–34] and the examples shown in section 3). Due to the practical problems of in-situ investigations and the difficulties in preparing suitable transparent HREM and TEM samples, the growth process itself can only be directly investigated if special UHV growth conditions are realized [35,36]. STM etc. (besides XSTM, the cross section variant of STM, cf. sect. 3.1) cannot access buried dots, but TEM alone is not sensitive enough for a composition analysis. Therefore a number of attempts have been made to determine, e.g., composition and strain by more direct quantitative HREM techniques based mostly on Fourier filtering of images or

lattice fringe distortion analysis (cf. the discussion in section 2.4). However, only a combination of all above mentioned methods with X-ray and electron diffraction methods (e.g., the convergent beam electron diffraction, CBED) as well as optical spectroscopy (photoluminiscence PL, cathodoluminiscence CL, Ramann spectroscopy, etc., cf. contributions of this volume) enable a complete structure analysis.

The HREM and TEM techniques have the difficulty of understanding the image features phenomenologically and quantitatively in terms of the investigated structures. Especially the separation between strain and shape related contrast features is difficult. Therefore the application of theoretical contrast modeling and image matching is unavoidable to determine the experimentally non-recoverable data and to get a unique structure analysis. Sections 2.2 and 2.3 are dealing with the simulation techniques in TEM and HREM, respectively, to provide a basis for the interpretation of the experimental results given in section 3. However, the simulation of HREM and TEM images of nanometer scaled objects demands a structure modeling on an atomic scale valid for microscopic relevant dimensions. Therefore in section 2.1 a short description of the modeling of QD structures is given, using molecular dynamics (MD) and molecular statics calculations, to get models for the image simulations. The subsequent simulation of HREM images based on such models yields a strong modification of the electron microscope image contrast revealing the strain field around the QDs. The main differences in the image contrast between relaxed and unrelaxed QDs (cf. one of the first papers using molecular static energy minimization with many-body cluster potentials for the modeling and image simulation of pyramidal shaped QDs in the InGaAs-system [7]) are a virtual truncation of the QD shapes and strain induced black-white lobes in cross-sectional HREM images, which may be the reason that mostly rounded dots occur in cross-sectional images. For technical reasons, in [7] it was impossible to calculate the plan-view images, too. But the diffraction contrast was simulated for the cross-sectional orientation, allowing one to discuss the depth dependency of the contrast of the pyramids and the possibilities and limitations of the size and shape analyses, bestowing great caution on interpreting the images. Not reflecting these results, in different papers [8,37–46] the same caution is demanded and the necessity is demonstrated of suitable model and image simulations. Thus, in the following, MD simulations and static relaxations mainly of InGaAs QDs in a GaAs matrix are discussed to gain a better understanding of the structural modifications due to relaxation and of the resulting TEM and HREM contrast modifications. The present overview is based on the experimental investigations described in detail in [4,5,47–55], selected results of TEM investigations are given in sections 3.1-3.3.

2 TEM investigations of quantum dots (QDs)

TEM/HREM image interpretation requires a theoretical structure modeling and the subsequent simulation of image contrast in order to understand the obtained features and to provide contrast rules. The present section summarizes the relevant techniques. Therefore in the following section 2.1 the basis of MD modeling is sketched to provide the application of image simulation and analysis presented in sections 2.2 (TEM-DC), 2.3 (HREM), and 2.4 (Quantitative HREM).

2.1 Empirical molecular dynamics structure simulations of QDs

To provide structural models on an atomic level with macroscopic relevance the methods of empirical molecuar dynamics (MD) are applied. While, in principle, it is now possible to predict material properties by using quantum-theoretical ab initio calculations with a minimum of free parameters, MD is the only method for simulating time-dependent atomic processes with sufficient particle numbers. Modeling electronic properties by, e.g., 8-band $\boldsymbol{k.p}$ theory gives good results if the effective mass or continuum description is sufficient. If continuum models of the structures are available one yields, e.g., the wave function and band structure of QDs sensitively depending on the strain distribution [2,6] and PL spectra as a function of strain and temperature [56–58]. For multi-band coupling and if the atomic structure is relevant (as, e.g., for the TEM and HREM investigations) one should better use ab initio methods, which, however, are restricted in the number of atoms too small for real QDs, even using special order-N pseudopotential methods and evaluating energy levels solely near the band gap [59].

The method of empirical molecular dynamics solves Newton's equations of motion for a molecular system using suitably fitted many-body empirical potentials. Such simulations enable a large number of particles ($10^5 - 10^7$ on workstations) and sufficient relaxation times (10-1000ps) to be considered. Evaluating the resulting trajectories for all particles yield the dynamical properties of the system, the relaxed configurations provide structural models for the simulation of TEM images and other static properties. The calculations are performed with a fifth-order predictor-corrector algorithm using a constant volume (NVE ensemble) or a constant pressure (NpT ensemble) and time steps of the order of 0.25 fs to ensure the proper calculation of all possible modes. NVE is preferred for free surfaces or simulations to calculate diffusion constants, whereas NpT enables the relaxation of the cell dimensions and the application of an outer pressure, which is important for, e.g., the reordering process at interfaces. For controlling the system temperature either all particle velocities are slightly rescaled at each time step, or solely the outer layers of the model, which enables the control of energy dissipation into a macroscopic environment. Alternatively to MD for structures near

the equilibrium, static energy minimization may be performed using steepest descent or conjugate gradient methods to relax structures towards one of the nearest local energy minima. In general, not revealing the global minimum and thus insufficient to describe reordering of the structures and their stability, the relaxed structures are suitable for TEM image calculations.

The interatomic forces in covalent solids can only sufficiently be described if the influence of the local environment according to the electronic structure is included. Simple pair potentials and potentials of the valence force field or related types as, e.g., the Keating (K) potential [60], are restricted in their validity to small deviations from the equilibrium. Especially for strain analysis in small dots its applicability may be questionable [61]. However, empirical potentials have been developed, which allow the calculation of the many-body interaction sufficiently well. Such potentials are mostly of the Stillinger-Weber (SW), the embedded atom approximation (EAM) or the Tersoff type. They offer advantages and disadvantages in the range of validity, physical meaning, fitting and accuracy as well as applicability [62]. Restrictions exist for all empirical potential types, even if special environmental dependencies are constructed to enhance the elastic properties near defects. In addition, all potentials are not well applicable to long range interactions, and the electronic structure and the nature of the covalent bonds can only be described indirectly. Therefore, it is of importance to find physically motivated semi-empirical potentials and to use suitable methods to fit to first principle as well as experimental data bases. The potential of Tersoff [63,64] is a bond-order potential, thus having a completely other functionality than simple many body interactions. The different parametrizations (TI, TII, TIII) of the Tersoff potentials are intensively tested in applications and an analytic derivation from tight-binding approximation exists [65] as well as an own parametrization of an extended bond order potential similar to [66], applied for diamond in [67]. However, for the present MD calculations SW (CdZnSe) and TII (InGaAs, Ge) is applied [64], whereas the static relaxations are performed with the Keating potential as given in [61], and by using the simple many-body potentials of the CERIUS [68] program package.

The atomic structures of InGaAs-QDs in GaAs matrix (and similar CdSe in ZnSe [41] or Ge in Si, etc.) are prescribed by geometric models as demonstrated in Fig. 1. Very different dot shapes have been proposed and theoretically investigated as, e.g., lens-shaped dots, conical islands, volcano type QDs, and pyramids with different side facets of type $\{011\}$, $\{111\}$, $\{112\}$, $\{113\}$, $\{136\}$, and both $\{011\}+\{111\}$ mixed, etc. Some of the different QDs used with facets $\{011\}$, $\{113\}$, mixed $\{011\}+\{111\}$, and a spherical cap are schematically presented in Fig. 1a. The most important difference of the various structures consists in the varying step structure of the facets due to their different inclination. Other configurations as shown in Fig. 1a are also simulated, and one or two monlayer (ML) thick wetting layers are compared with calculations not using wetting layers. The importance to investigate such con-

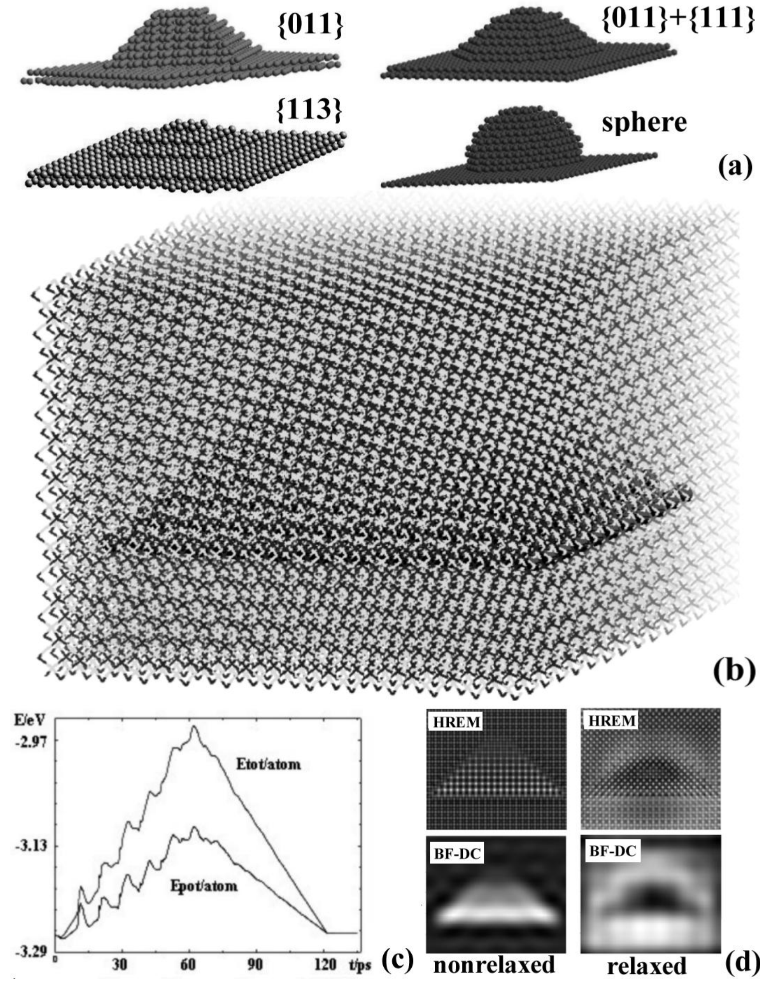

Fig. 1. Structure modeling and image simulation of different pyramidal-shaped quantum dot configurations: a) different facetting, truncation, and wetting of pyramidal start models (matrix removed, models related to (001)-base planes), b) relaxed complete model of a {011} pyramid (base length about 6 nm, $10 \times 10 \times 10$-supercell length 10 nm), c) energy relaxation of a {011} quantum dot (potential E_{pot} and total E_{tot} energy versus time steps), d) cross-section HREM and e) BF-DC before and after relaxation simulated for model (b) at Scherzer focus $\Delta =$ -40 nm (parameter cf. section 2.3: 400 kV, $C_s = 1$mm, $\alpha = 1.2\,\text{nm}^{-1}$, $t = 9\,\text{nm}$, $\delta = 8\,\text{nm}^{-1}$).

figurations has at least two reasons. First, small embedded precipitates have always facets; a transition between dome-like structure and pyramids, e.g., due to changes in spacer distance, change the number and arrangement of the facets, and thus strain and electronic properties [23,39,45,46,69]. Second, for highly facetted structures the continuum elasticity is practically inapplicable and FEM calculations must be done in 3-D instead of 2-D [42–46,69]. The embedding of one perfect $\{011\}$ pyramid in a matrix is demonstrated in Fig. 1b after prerelaxation. Fig. 1c shows a typical annealing behaviour during empirical MD calculation, characterized by the potential E_{pot} and the total energy E_{tot} per atom. The energy difference $E_{tot} - E_{pot}$ is equal to the mean kinetic energy and thus directly related to the temperature of the system. After the prerelaxation of 5ps at 0K, an annealing cycle follows, 60ps stepwise heating up to 200K and cooling down to 0K, with equilibrating the system at each heating step. The example demonstrates a short cycle, mostly the embedded QDs are relaxed at each T-step for at least 10000 time steps of 0.25fs, i.e. for 250ps, and annealing follows up to about 600K, which is not well defined for empirical potentials but below the melting temperature (the details will be published elsewhere, cf. [41] and in forthcoming papers). The simulations of the stability of the QDs are valid as long as no direct interaction occurs between In and Ga (Cd and Zn) during intermixing or diffusion, and should be enhanced using better potentials. Whereas the structure in Fig. 1b is less strained, highly strained configurations occur due to the self-interaction of the QD in small supercells which corresponds to a stacked sequence with very small dot distances. The starting configurations for the smallest QD are supercells in $\langle 100\rangle$ orientation of $13 \times 13 \times 13$ unit cells with 17576 atoms and a resulting box length of 7.2 nm. The base length of the dots is about 6 nm. In $\langle 110\rangle$ representation, necessary for using the simulations in respective HREM investigations, the structure is changed by a $1/\sqrt{2} \times \sqrt{2} \times 1$ supercell transformation and contains 16848 atoms (due to different periodic continuation). Alternatively, larger cells with the same QD ($17 \times 17 \times 1$, box length 8.8 nm or 9.4 nm, 30976 atoms) and smaller dots within the $13 \times 13 \times 13$ boxes (base length 5.3 nm) and the respective transformations are used to investigate effects of the self-influence of a QD in smaller cells due to periodic boundary conditions. The smaller structures are relaxed using MD as described above. In addition, $20 \times 20 \times 20$ supercells (11.1 nm boxlength) are constructed in the same manner for testing different sizes and shapes of the QD. Here and for the large QD the structures are relaxed by static energy minimizations only. The starting configurations for the large QD are $51 \times 51 \times 51$ and $89 \times 89 \times 89$ supercells solely in [100] orientation with base length of the QD of 7 nm and 9 nm, respectively. For the image simulations subregions are used of $71 \times 71 \times 71$ supercells maximum. By comparing imaging for structures before and after relaxation, Figs. 1d and e) demonstrates the enormous influence of the relaxations to the image

contrast in cross-section HREM and TEM, resp., as discussed in detail in the following sections.

2.2 Analysis of QDs by conventional diffraction contrast

The method of electron microscope diffraction contrast (DC) is a particular imaging technique, also called conventional TEM, where only the primary beam (bright-field image, BF) or one of the beams diffracted by the distorted crystal (dark-field, DF) is selected by the aid of the objective aperture (contrast diaphragm). Plan-view TEM images allow to determine not only the size distribution and dot density, but also the relation between adjacent islands. Fig. 2 (upper part) shows a typical micrograph of InAs dots on a $\langle 001 \rangle$ GaAs substrate, with varying contrast across the bend contour due to changing excitation conditions. Near the centre of the image the specimen is exactly orientated in the $\langle 001 \rangle$ zone axis. Due to the conventional diffraction contrast technique applied, the dots are detectable mainly by their strain fields. In this case the size of dots, however, would be slightly overestimated (cf. the contrast rules discussed below). From contrast analyses it can be concluded that the dots seem to have a rectangular base face and edges in the base along $\langle 100 \rangle$ directions. In this particular case, the dot density reaches about 10^{11} cm^{-2}, the islands themselves have distances of about 250 Å, preferentially arranged in specific crystallographic directions. As discussed in the following, small inclusions in a crystalline matrix can be analyzed in diffraction contrast TEM micrographs by chosing so-called two-beam conditions. As an example, Fig. 2 (lower part) presents a series of bright-field images, where three different Burgers-vectors $\mathbf{g}$ were excited. Islands are characterized by a lobe contrast of mirror symmetry.

In such TEM-DC no true images are formed, therefore a phenomenological interpretation of the contrast is nearly impossible. The information on the periodicity of the lattice is lost. Therefore the analysis of DC contrast images demands image simulation or image matching based on the dynamical theory of electron interferences. However, the long experience of image interpretation and the wide variety of calculations available in the literature enable the application of rules describing contrast effects under particular imaging conditions, as, e.g., inivisibility conditions to determine Burgers vector of dislocations and translation vector of stacking faults, but also symmetry rules of BF and DF, oscillation behaviour and the contrast maxima during tilt of the samples (for practical use cf. [70]). The contrast rules cannot be applied without a priori knowledge about the defects or if the defects are not clearly imaged in perfect two beam excitation. Quantum dots are considered to be a special case of 3-dimensional (3-D) defects like clusters of point defects, small dislocation loops, stacking fault tetrahedra, and small precipitates. The extension of such defects is an important contrast determining parameter. Point defects may be included here as the special case of very small 3-D crystal de-

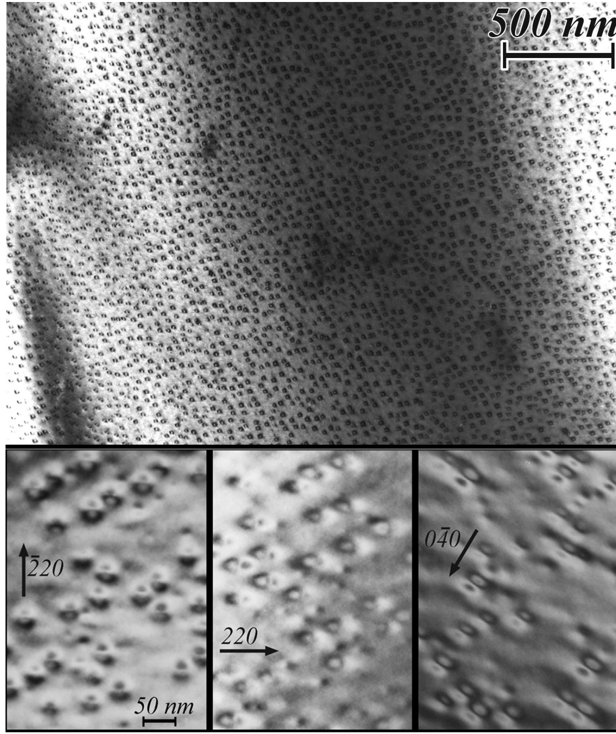

Fig. 2. Upper part: Bright-field TEM image of a single layer of InAs dots grown on a ⟨001⟩ GaAs substrate by MBE (Ioffe Institute, St. Petersburg). In this case the islands often appear as dark contrast dots having a bright center. Lower part: Bright-field two-beam images of InAs islands on a ⟨001⟩ GaAs substrate for different **g**-vectors indicated by arrows.

fects. However, they cannot be imaged directly in TEM and HREM because of their small strain fields.

The most important effect of such small 3-D defects is the strain contrast caused by the deformation of the surrounding matrix. The direction and the amount of the elastic strain determine the contrast properties, whereas the lattice structure and the difference in atomic scattering factors have only a small influence. The lattice structure is negligible because the small QD can be understood as homogeneous precipitates not showing interface contrast nor moire fringes. The structure factor contrast is in a first order approximation equivalent to an effective thickness change of $R_o(1/\xi_o - 1/\xi_m)$, which is a negligible effect for typical QD radii of about $R_o = 15\,\text{nm}$ (the extinction distances of matrix ξ_m and dot ξ_o are about 16 nm -30 nm for GaAs in the 2-beam approximation for (111) and (200) reflections). Following the discussion of Chick et al. [71], Lepski [72], and others (see, e.g. [73] and references therein), the strain contrast in a two beam excitation may be approximated analytically in first order perturbation and by using the Ashby-Brown [74] displacement field of a spherical inclusion in isotropic media.

The different investigations may be summarized to a diagram as given in Fig. 3 [73]. The grey shaded area characterizes typical QDs with constrained strain ε corresponding to a misfit between 0.6% and 6.0% and radii

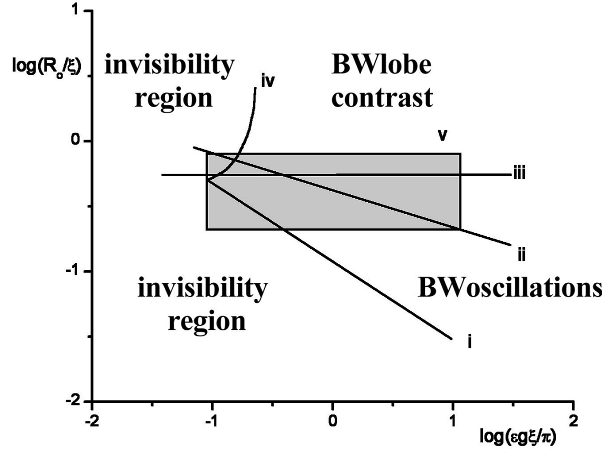

Fig. 3. Schematic representation of the visibility and typical contrast features of small spherical particles by strain diffraction contrast (after [72,73]): (i,iv) limit of visibility of small and large QDs, resp., for a fixed reflection, (ii, iii), lower and upper bound of black-white oscillation contrast, resp. (cf. text), (v) confidence region for a typical QD with radii $6\,\text{nm} < R_o < 15\,\text{nm}$, characteristic two-beam extinction lengths of GaAs $16\,\text{nm} < \xi < 30\,\text{nm}$, and misfit between 0.6% and 6.0%.

$6\,\text{nm} < R_o < 15\,\text{nm}$, by using parameters of GaAs $16\,\text{nm} < \xi < 30\,\text{nm}$. The maximum contrast of a particle is obtained approximately at 0.4ξ apart the centre and drops down exponentially outside. Dots are invisible for very small particle diameters $2R_o$ or for small strains ε. Using a 10% contrast rule with respect to the background and exact two beam orientation, the visibility limit is approximately $g\varepsilon R_o^2/\xi^2 = 0.1$ (curve i). A more complicated rule exists for large particles (curve iv), which are invisible due to decreasing strains [72,73]. However, very large particles may be considered as separate phases, and the contrast is determined by the effects neglected above: interface, moire or structure factor contrast. Particles with $g\varepsilon R_o^3/\xi^3 < 0.2$ create typical black-white (BW) contrast with depth oscillations (curve ii, lower bound [75]). For $R_o > \xi/2$ (curve iii, upper bound [72]) a black-white contrast without oscillations, also called black lobe or coffee bean contrast is obtained (see also Fig. 2). The BW contrast can be denoted by a characteristic vector $\boldsymbol{l}$ pointing from the black contrast to the white one. Orthogonal to the BW vector a line of no contrast exists between the black and white lobes. The changing sign of $\boldsymbol{l}$ as a function of the depth below the surface describes the BW oscillations. For depth positions equal to $\xi/2$ and for defects in distances greater 2ξ from surfaces, black dot contrast arises ($\boldsymbol{l} = 0$). For all black lobe contrasts and for particles showing BW oscillations but lying in a distances

of less then $\xi/4$ from the surfaces, the Ashby-Brown rule holds: $\boldsymbol{l}$ is parallel $\boldsymbol{g}$ for compression $\varepsilon > 0$ and antiparallel for dilation $\varepsilon < 0$. Near the entrance surface the Ashby-Brown rule is valid for BF and DF, near the exit surface the direction of $\boldsymbol{l}$ is retained for DF but reversed for BF. The rules fail for BF near symmetrical incidence, and have to be modified in detail for particles with non-spherical shapes and matrices with strong elastic anisotropy. An interesting phenomenon obtained in the CdZnSe system with QDs of about 10 nm base length is reported by Litvinov et al. [28]: The coffee-bean contrast of the strain field is accompanied by stacking- fault fringes, which are best visible under weak-beam contrast conditions. In [76] contrast imaging with apertures between all reflections is proposed to enhance the shape and size recognition and to suppress the strain contrast. Whereas the principal contrast effects are retained, especially thickness and depth behaviour, the far-field contrast lobes are modified mainly by the elastic anisotropy, and all structural details characteristic for the particles shape can only be understood by using image simulations. Such simulations based on Mura's displacement field [8] for spherical inclusions in anisotropic media are applied to demonstrate that the contrast of spherical particles may show square edges, too. However, the experimental micrographs in [7,8,37] cannot be explained sufficiently by the contrast of the spheres because of the much sharper edges and corners shown in the experiments. This holds also for uncapped dots as, e.g., in [38,39], for which further detailed investigations are necessary.

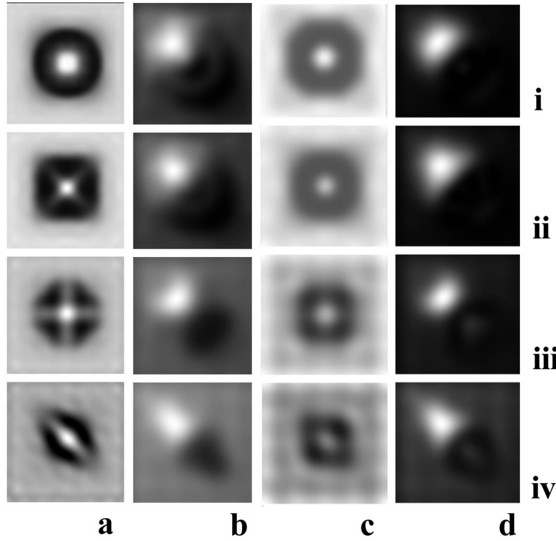

Fig. 4. Simulated 200kV bright-field (a,c: BF, 6 nm^{-1} aperture) and dark field of the 220-reflex (b,d: 220-DF, 3 nm^{-1} aperture) of the large quantum dot (base length 12 nm) relaxed by static energy minimization for a sample thickness of a,b) $t = 23$ nm and c,d) $t = 34$ nm and different facetting: i) lens shaped dot, ii) {011} pyramid, iii) {113} pyramid, iv) {136} pyramid.

In contrast to [7], the image simulation applying only one parameter set in [8] is thus insufficient for a unique contrast interpretation. Though it had

been shown in [7,8] that the strains seem to be the most important contrast determining factor, the shape of the dots, the facetting, the thickness of capping layers, and the existence and thickness of wetting layers are important and change the strains itself. Particularly small spheres have a large number of differently oriented facets. Thus, simulations using only spherical inclusions or displacement fields in isotropic media cannot explain the HREM images of non-spherical structures and the influence of anisotropy, respectively [40]. Here, better results may be revealed using the diffraction contrast analysis of non-spherical inclusions [77], cubes or ellipsoids in anisotropic media [72], or applying finite element methods (cf., e.g., [78,40,44] but restricted to conical islands and neglecting the modified BF) to evaluate the strain fields. The calculations in [25] reveal the contrast inversion with increasing thickness and the sensitivity to imaging conditions as discussed above. The modeling nevertheless seems to be done using continuum models in many beam imaging. In contrast to [8] clearly disks and plates may be discriminated, especially in BF and 400-DF for good resolution. However, as mentioned above, the facets cannot be reflected simply by continuum methods. Therefore, based on MD relaxed structure models (cf. section 2.1) simulations are performed by the HREM option of the CERIUS package [68] or the EMS software [79], where only the latter one enables to divide the larger supercells into a sufficient number of subslices (more than 100). To avoid image artefacts, at least 4 subslices per unit cell in [100] direction should be used for weakly distorted structures, which correspond to a slice thickness of $\Delta t = 0.1417\,\mathrm{nm}$. The ratio of the absorption potential is assumed to be 0.05 and the Scherzer defocus is chosen in all diffraction contrast simulations. The imaging aperture is varied between $2\,\mathrm{nm}^{-1}$ and $6\,\mathrm{nm}^{-1}$ to have sufficient information of the QD itself and to avoid image artefacts due to higher order Laue zone reflections. These may result if atoms with larger shifts according to the elastic strain field are misplaced periodically in different slices of the supercell.

Fig. 4 shows simulated zone-axis bright-field contrast (BF: a,c) and the [220]-dark field images (DF: b,d) of the large QD (base length 12 nm) with different facets (cf. Fig. 1 for the shapes): lens shaped QD and pyramids with {011}, {113}, and {136} facets from top to bottom, respectively. Two different sample thicknesses were chosen: $t = 23\,\mathrm{nm}$ in (a,b), and 34 nm (c,d). The simulations reveal that there are zone-axis BF imaging conditions for thinner samples that allow a clear distinction of the different QDs by their characteristic contrast features, whereas all DFs are dominated by the BW-contrast features.

A similar series of simulated zone-axis bright-field micrographs for the small dot with a base length of 6 nm is shown in Fig. 5. The shape evaluation is much more difficult and the contrasts show a lot of details probably due to the very low defocus spread assumed for the imaging with the 200kV field emission microscope.

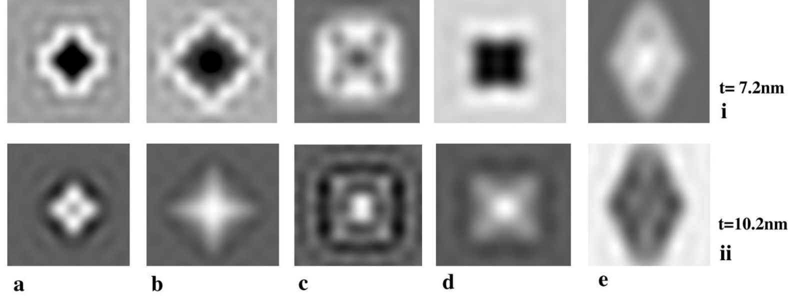

Fig. 5. Simulated 200kV zone-axis bright-field images (BF, $6\,\mathrm{nm}^{-1}$ aperture) of the small quantum dot (base length 6 nm) relaxed by MD energy minimization for a sample thickness of i) $t = 7.2$ nm and ii) $t = 10.2$ nm and different facetting: a) {011} pyramid, b) {011} pyramid truncated, c) {112} pyramid, d) {113} pyramid, e) {136} pyramid.

Thickness variations of the BF diffraction contrast are dealt with in Fig. 6 for a single sphere with a diameter of 5 nm (i) and the {011} + {111}-pyramid with 6 nm base length (iii) as well as stacked configurations of (i) and (iii) in (ii) and (iv), respectively. The sample thickness t varies from 32 nm to 122 nm (a-e in i,ii) and from 54 nm to 136 nm (a-e in iii,iv). Besides the contrast reversal a different visibility of the shapes may be revealed with increasing thickness. However, there is a strong influence of beam tilt, imaging aperture, etc., whereas the defocus only slightly change the contrast. Large defoci, as demonstrated by $-1\,\mu$m in Figs. 6f, modify the detail visibility and yield to additional Fresnel fringes.

The figures demonstrate clearly the sensitivity of the theoretical contrast with parameter variations, even wrong virtual shapes may occur for simulations using to small apertures. Without strains solely a weak structure factor contrast arises. Even though the lens-shaped QD shows slight deviations from rotationally contrast symmetry, the pyramids clearly can be distinguished by the sharpness of the basic feature and the additional occurance of contrast fringes along the ledges of the pyramids. The pyramidal QDs with a steeper descent of the facets show a fourfold symmetry of their contrast features. These, however, are clearly visible only at a symmetric bright-field incidence. The striations superimposed show that here some of the structures are not yet completely relaxed, especially at the borders of the supercell, leading to contrast artefacts due to the structure continuation for larger thicknesses, their contrast depends sensitively on the objective aperture chosen. A further increase of the thickness lowers the visibility of the clearly visible features for shape discrimination.

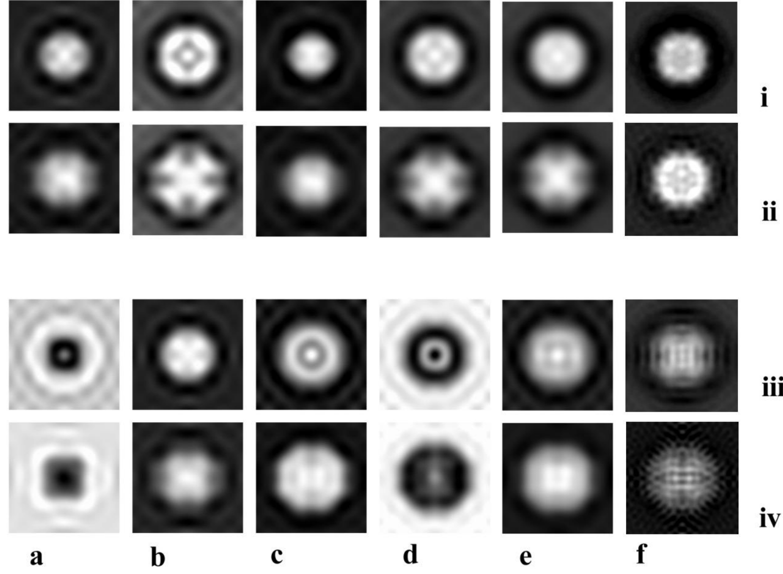

Fig. 6. Influence of sample thickness t to the BF-zone axis diffraction contrast: i) single sphere of radius $R_o = 5$ nm, ii) 011+111 mixed pyramid with 6 nm base length, iii), iv) stacked arrangements of i, ii), respectively; $t = 32$ nm, 50 nm, 68 nm, 86 nm, 122 nm (a-e in i,ii); $t = 54$ nm, 72 nm, 90 nm, 109 nm, 136 nm (a-e in iii,iv), f) as e) with large defocus of -1µm.

2.3 Analysis of QDs by phase contrast

The phase contrast in HREM imaging is created by the interference of a sufficiently large number of diffracted beams leaving the exit surface of the sample and passing the contrast aperture (with half angle α) in the diffraction plane. For each of the diffracted beams similar considerations are possible as done for the DC discussed in section 2.1. The higher resolution using many beams enables imaging of single or pairs of atomic columns and a reduction of the strain contrast in the background is obtained. However, the contrast is always strongly modified by the imaging process of the microscope itself. The imaging process may be considered as a twofold Fourier transform according to Fraunhofer diffraction and a convolution with the wave transfer function. A complete image calculation includes non-linear beam interactions, defocus Δ, beam tilt, and at least image aberrations: spherical C_s and chromatic astigmatism, threefold astigmatism and coma. In addition, the microscope instabilities are included at least as defocus spread δ and beam divergence θ. The object wave simulations are performed by the HREM option of the CERIUS package [68] or the EMS software [79], as described above for DC calculations, and must be complemented by the simulation of the imaging process. The imaging parameters are chosen according to two typical microscopes,

the JEOL 4000EX at 400 kV accelerating voltage used for high resolution microscopy and the Philips CM20 FEG with 200 kV equipped with a field emission gun: accelerating voltage $U = 400$ kV (200 kV), spherical aberration $C_s = 1.2$ mm (1.0 mm), defocus spread $\delta = 8$ nm (5 nm) and beam divergence $\theta = 0.05$ mrad (0.03 mrad).

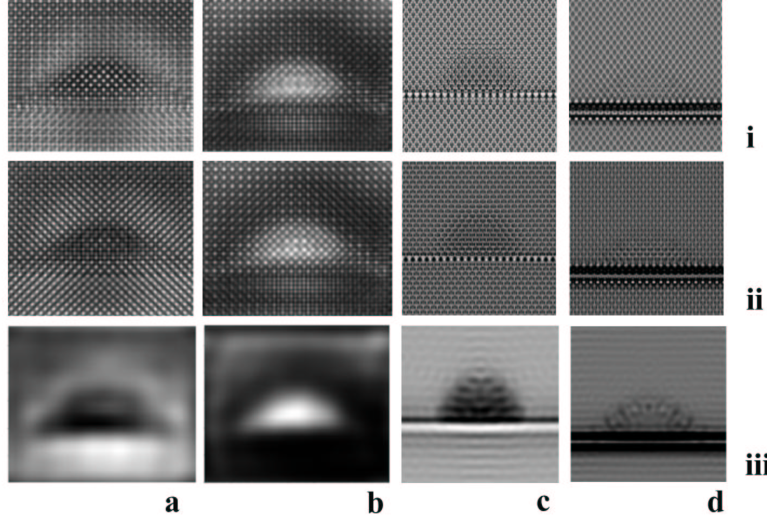

Fig. 7. Series of simulated cross-section 400kV HREM (row i,ii) and corresponding BF-DC images (row iii) of QDs in InGaAs: [100]-view (a,b) of a {011}-pyramid (model of Fig. 1b), and [110]-view (c,d) of a spherical cap (c) with $R_o = 2.5$ nm and a mixed {011} + {111}-pyramid (d). Defoci $\Delta =$ -40 nm (i:a,b),70 nm (ii:a,b), -25 nm (i:c), -30 nm (ii:c, i:d), and -35 nm (ii:d). Foil thickness: $t = 13.6$ nm (a), 22.6 nm (b), 41 nm (c), and 169 nm (d). (400 kV, $C_s = 1$ mm, $\alpha = 1.2\,\text{nm}^{-1}$, $\vartheta = 8$ nm, $\theta = 0.05$ mrad).

Fig. 7 shows in (a,b) simulated cross-section HREM micrographs for different defoci and thickness (for the details cf. Figure caption) of the InAs-{011} pyramid in GaAs in comparison with cross-section BF images selected from [7]. Analogous simulations for the [110]-orientation of a spherical cap and a mixed {011} + {111}-QD are presented in Figs. 7c,d, respectively. As discussed in [7,41,80] for HREM of QDs in InGaAs and CdZnSe, the most important effects are the visibility and large influence of the strain, and that the pyramidal dots always look truncated. Between 15 nm and 20 nm thickness a first contrast reversal occurs. Larger thickness reduces the visibility of very small dots in HREM and zone-axis BF patterns limiting the range of suitable defoci for enhanced contrast. The strong influence of thickness, depth position, and defocus needs always careful determination of the imaging con-

ditions and/or the application of quantitative image matching as discussed in the next section.

2.4 Quantitative analysis

A quantitative analysis of all structural QD properties has to combine different experimental imaging and spectroscopic techniques. By restricting to solely considering the TEM/HREM imaging, a quantitative analysis here consists in image matching by repeatedly applying the techniques of MD-modeling and image simulation as described in sections 2.1 to 2.3 (direct or inverse object retrieval is not yet practically available, cf., e.g., several contributions in J. Microscopy 1998, Vol. 190). In addition, the quality of the trial-and-error refinement of model, scattering, and imaging parameters has to be evaluated by fitting a likelihood or R-factor criterion (cf., e.g., [81,82]). However, the application of the extensive image matching techniques prior the existence of sufficiently well modeled QD structures does not solve the problems. Therefore a large variety of image processing techniques are applied instead, which yield directly strain, composition and/or thickness patterns by suitably filtering out the relevant information. One of the first proposed methods of quantitative analysis of the information from transmission electron micrographs (QUANTITEM, cf. the overviews [83–86]) transforms the high- dimensional space of information contained in characteristic image templates to such a 3- dimensional vector which is most sensitive to thickness and composition variation. The comparison with templates of known composition enables a calibration and thus an interpretation of the local variation of the 3-D information as chemical mapping. **D**igital **a**nalysis of **l**attice **i**mages (DALI [82]), **la**ttice **di**stortion **a**nalysis (LADIA [31]), and all comparable investigations (cf., e.g., [87,88]) are real space methods analysing the relative lattice fringe distorsion in images by comparing them with undistorted regions either pixelwise or by evaluating intensity maxima with subpixel accuracy. In contrast, the **c**ompositional **e**valuation by **l**attice **f**ringe **a**nalysis (CELFA [89,22]), and similar methods [90,85,91], where imaging conditions are used, which enable maximum sensitivity of the image contrast via the chemical {002}-reflection, provide the composition pattern by Fourier analysis and filtering techniques. Fuzzy logic and neuronal networks [92,93] in addition apply respective pattern recognition techniques to analyse the compositional and thickness information. The improved CELFA [22,23,94] shows that under appropriate 3-beam imaging conditions the intensity ratio of the {002} and {004} reflections is proportional to the In-content in the InGaAs system; using defocus series, all additional parameters may be estimated and concentration gradients in dots and wetting layers are measurable. Finally, holographic imaging should be mentioned, which enables directly to evaluate amplitude and phase of diffracted electron waves, which in the two first applications [95,96] is used to determine quantitatively the change of the

mean inner potential in QDs and that large dots in InGaAs are pyramids with rounded edges and top.

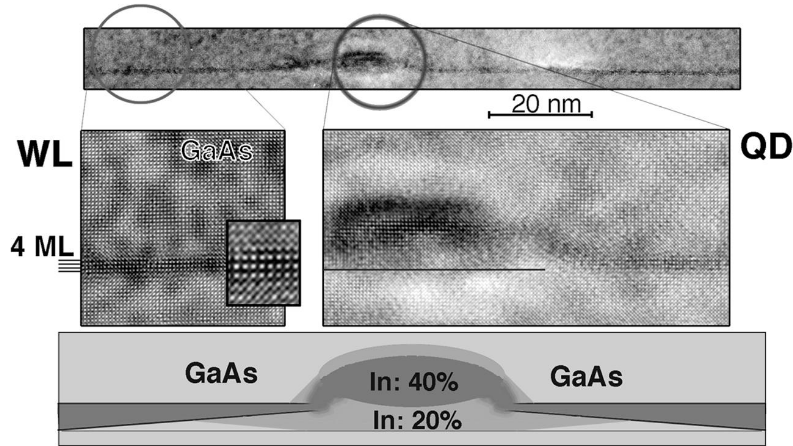

Fig. 8. Analysis of a single layer of InAs QDs: Upper part cross-section image. Middle part HREM image of the wetting layer (WL) consisting of 4 monolayers of InAs. Lower part schema of the inhomogeneous In distribution in the island. The chemical analysis (distribution of In) is obtained from image processing ({200} filtering). Sample: TU Berlin.

Fig. 8 demonstrates the situation of a single layer of InGaAs dots grown by MOCVD [16], where the In distribution has been analyzed in the island as well as in the InAs wetting layer. The upper part shows a cross-section image of the island at lower magnification. Two sections (circles) have been analyzed by image processing of the corresponding HREM micrograph (middle). The information of the chemical composition has been derived from analyzing the {002} reflected beam, which is chemically sensitive to the shape of different atomic species in the sphalerite-type sub-lattices for crystallographic reasons. Due to the complex lattice distortion at the islands, the accuracy and the local resolution of this method is restricted (in this case: $\pm 10\%$). However, it is obvious that within the island the In concentration is shifted to the upper region (maximum 40%). Moreover, the In in the surrounding wetting layer is consumed during the further growth of the island caused by a post-annealing step. Such an interdiffusion-related changing of size and stoichiometry of islands has a direct influence on the emitted wavelength detectable by PL measurements.

3 Structure Investigations of Quantum dots

After the discussion of TEM contrast phenomena of QD islands, the present section deals with the application of the above mentioned imaging and simulation techniques. During the last decade electron microscopy has been successfully used for the analysis of nanostructures, especially of QDs of numerous semiconductor materials systems. Here only some specific examples can be presented, which demonstrate the general use of these methods as a survey of their possibilities and limitations. Always one should keep in mind that only some combination of the above-mentioned techniques allow the successful morphological analysis of QD structures, their growth phenomena and optical behaviour.

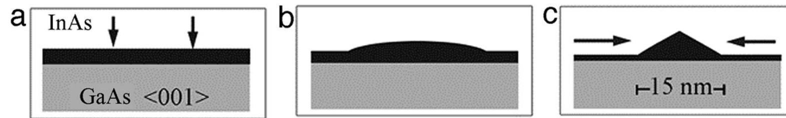

Fig. 9. Scheme of different growth steps of the island formation in the lattice strained InAs/GaAs system: a) pseudomorphous layer growth for deposited thickness below 1.7 ML, b) island formation for $>$ 1.7 ML deposition, c) pyramid formation due to surface diffusion.

Since most of the presented examples refer to investigations of structures in InGaAs systems, the specific generation of islands should be briefly mentioned again, although it has been described in detail in other chapters of this book. Fig. 9 presents some basic features of the formation of InAs dots/islands on a GaAs substrate grown via the Stranski-Krastanow mode obtained from TEM investigations. The first deposited monolayer (ML) creates a pseudomorphous closed layer (wetting layer, WL), which is strained due to the lattice misfit (7% for InAs/GaAs). During a further deposition ($\approx$2ML) small islands are forming (b). This transition from the layer growth to the island formation results from a complex process controlled by strain, kinetics like surface diffusion, and the incorporation of ad-atoms. As an example, TEM investigations have shown that specific growth interruptions (few seconds to some minutes) cause island growth and a consumption of WL material around the islands (Figs. 9b$\rightarrow$c) [97]. The interaction between surface strain fields and growth energetics is predicted to improve the lateral ordering [98,99]. Owing to the growth parameters and techniques applied, different shapes of islands occur, varying between flat pyramids and spherical islands. During further growth, the islands are usually covered with a GaAs coating/capping layer. As a result of a complex diffusion process the island shape is transformed, for instance, into a truncated pyramid. While AFM investigations show only a specific situation of the islands at the surface, TEM enables one to correlate optical measurements with structural features.

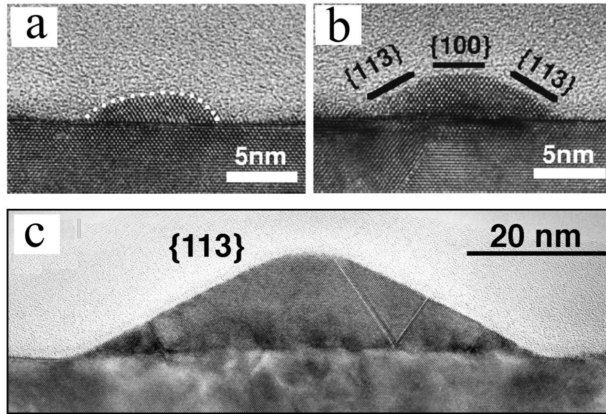

Fig. 10. Cross-section HREM images of Ge islands on a Si substrate with different shape. a) first state of island formation, b) small dome-like island with facets, c) large pyramid with {113} facets including a misfit dislocation.

At first some specific features of uncapped islands will be shown as represented by Fig. 9 b and c. The following section demonstrates the morphological changes during a subsequent capping of the QD by a matrix layer. This concerns not only the morphology of the islands, but also the modification of the wetting layer. Later the situation of stacked structures will be discussed. For the InGaAs system, the scientific interest and technological aim is focused on QD arrays emitting light of about 1.3 to 1.5 μm, depending on the following parameters of the QDs: size, shape, lattice strain and chemical composition. All these specific parameters are combined in a complex way due to the thermodynamics and kinetic processes during the growth of QD samples. It is the aim of TEM techniques to separate these parameters of complex information, e.g., strain and chemical composition.

3.1 Single layer of uncapped and capped QDs (InGaAs, GeSi)

To measure the size and shape of free standing islands, different techniques can be applied. Especially atomic force or scanning tunneling microscopy (AFM, STM) have been successfully used in the Si-Ge system and semiconductor heterostructures [100,101] to study, e.g., the shape transition from small clusters to huts, pyramids and domes. However, for the interpretation of such micrographs one has to take into account that the received image is a superposition between sample morphology and the shape of the tip of the AFM/STM. Furthermore, small facets and edges are difficult to resolve. Here TEM techniques are able to measure such parameters with a higher accuracy. As an example, Fig. 10 presents HREM cross-section images of uncapped islands, showing different resulting shapes due to varying growth parameters. In Fig. 10a and b, two images of Ge islands on Si are presented, a system which has been intensively studied from the view point of both fundamental and applied science. In (a) the small island has a round shaped surface, whereas in (b) the island is facetted [49]. A larger pyramid is given

in Fig. 10c, where relaxation has started by generating a misfit dislocation. The HREM image demonstrates that this dislocation is situated in the interface additionally forming stacking faults on {111} planes. In the case of such larger islands it may be observed that at the base the wetting layer and some matrix material is consumed resulting in small ditches.

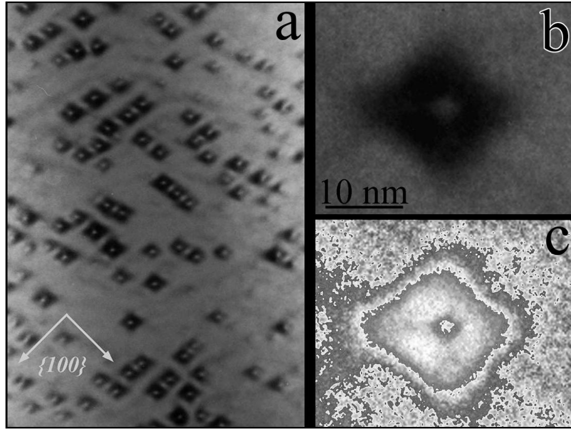

Fig. 11. a) Bright-field [001]-in-zone image of InAs dots on a GaAs substrate. The magnification of a single dot and its densitometer image (b) propose a rhombohedral-like shape (c).

The determination of the size and shape of QDs by plan-view diffraction contrast micrographs is possible under the restrictions discussed in section2.2. These contrast features, mainly caused by the strain field, correlate to the size of the islands (cf. Fig. 11). However, the exact size and shape of their bases cannot be extracted easily. Especially the actual size of islands is smaller than suggested. Different attempts have been made to gain this information by comparing the experimental images with the simulated contrasts based on specific island models. One experimental possibility concerns the analysis of TEM micrographs taken under suppressed-diffraction conditions [102] or taken in exact zone orientation. The latter case is also demonstrated in Fig. 11a-c. Fig. 11a) shows a bright-field image of InAs islands on a $\langle 001 \rangle$ GaAs substrate, where the sample is exact $\langle 001 \rangle$ oriented. Under these conditions the diffracted reflections are relatively weak as compared to those of strong two-beam excitation and the influence of the lattice strain on the image contrast is reduced. A magnified image of an island is seen in the upper right (b). A careful analysis of the contrasts reveales that, under these special growth conditions, the dots seemed to have a more rectangular or rhombohedral base as demonstrated by the densitometer analysis (c).

As demonstrated in the previous section of contrast simulation, such bright-field images with reduced influence of lattice strain allow the morphology analysis of dots of different size. As an experimental example, Fig. 12 shows the specific image contrast of three typical islands. In the beginning of island formation, InAs dots are often circular and flat (a), whereas later

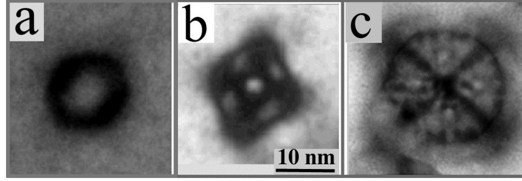

Fig. 12. Plan-view bright-field in-zone images of QDs of different samples. a) represent a capped InAs island of a single QD layer. A larger island formed in a multiple-stacked layer (b) has a more rhombohedral shape. c) uncapped Ge island of four-fold symmetry.

they are transformed to larger pyramides (b). A larger uncapped Ge pyramid is characterized by a four-fold contrast pattern (c), where the 4 dark lines correlate with the main edges. Besides on size and shape, the energy states of the excitons depend on the local chemical composition inside the islands. It is influenced, e.g., by the growth process and the post-growth annealing of the samples implying an interdiffusion of the elements between matrix and island. The change in stoichiometry as, for instance, the In/Ga ratio is revealed as an integral measurement using PL spectroscopy. Several approaches have been made to determine an element distribution in the sub-nm-range by image processing of HREM micrographs (cf. section 2.4). The application of these techniques to the analysis of QD structures is partly restricted, by, e.g., a superposition of the lattice plane images with local strain contrast. First of all one has to separate/eliminate lattice distortions, which would disturb the analyzing process. Second, a general problem of HREM image analyses is the separation of imaging parameters to gain independent information of them. This includes the determination of the local specimen thickness, imaging parameters as well as lattice strain fields.

Fig. 13 shows as an example the case of a HREM analysis of a 3-stack structure of InAs dots in a GaAs matrix. A lattice plane image (a) was taken at $\langle 001 \rangle$ sample orientation including the four chemical sensitive (200) reflections as well as four (220) reflections, respectively. At the lower dot-matrix interface an abrupt transition is observed, visible by the image structure change (Fig. 13 c), whereas on the upper interfaces the transition is quite smooth (b). The different structure pattern can be used to determine the local In/Ga ratio. As an example of such image processing techniques, Fig. 13d demonstrates a filtering process using the (200) reflection. The resulting information on the In/Ga ratio (Fig. 13e), however, is superimposed by strain. Taking into account the lens-shape of the dots, the In concentration and distribution can be estimated. The line scan yields an out-smoothing of the In during the growth process with a decreasing of the In concentration down to about 70%. However, the accuracy is limited to about 10%. Besides HREM image analysis, the energy-filtered TEM technique (EFTEM) has become well-established in recent years allowing chemical mapping with a lateral resolution down to the 5 Å range. In such element specific images even single

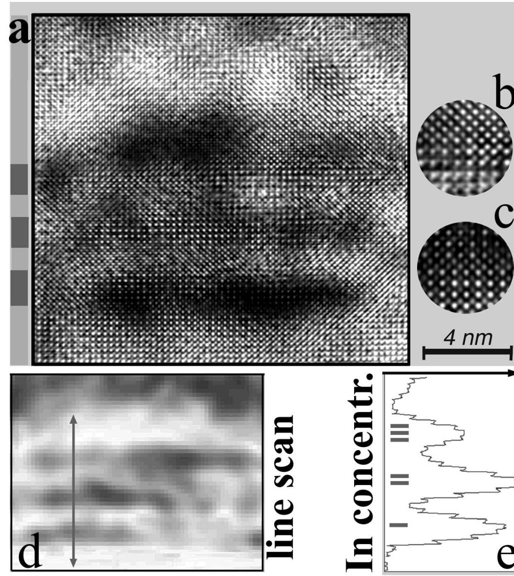

Fig. 13. Example of an image filtering procedure to extract the local chemical composition (In/Ga ratio): a) HREM image of a ⟨001⟩ oriented sample including a stack of 3 InAs dots in a GaAs matrix. b), c) magnified sections of the typical interface structure showing the transition between InAs and GaAs. d) After filtering the In content appears as dark region. A corresponding line scan shows the In distribution (e).

lattice planes are resolved. However, also in this case lattice strain fields have to be taken into account for a quantitative interpretation of the chemical distribution [103]. Fig. 14 presents such an EFTEM micrograph of a single InAs dot layer grown by MBE. The element map using the In signal is shown on the left, where the position of the island is marked by dots. The line scan on the right shows strong signals at the island, especially at the top of the QD marked by an arrow. Such an inhomogeneous In distribution occurs particulary in larger InAs/InGaAs dots.

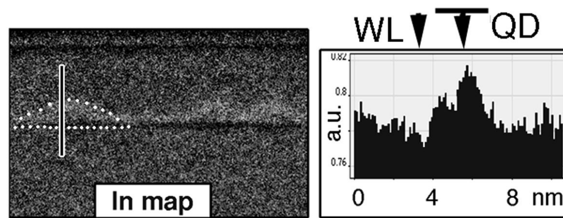

Fig. 14. EFTEM image of a single InAs dot layer using the In signal (left). The corresponding line scan (right) indicates an inhomogeneous In concentration throughout the island.

Since the detection limit of these TEM imaging techniques is restricted by the lattice distortions and the final thickness of the specimen, such an analysis should be combined with other methods. A promising project is to study the atomic and chemical structure of semiconductor nanostructures with STM imaging of cross-sections of the dot region prepared by cleavage [104].

3.2 Stacked QDs layers of InGaAs in GaAs

Optical properties of a single QD layer are characterized by a broad PL peak, which is related to the size distribution of QDs. To improve this situation (higher dot density, more pronounced size distribution) promising solutions have been developed, two of which will be mentioned. First, multiple stacking of QD layers has been envisaged as an attractive growth concept to provide a 3-dimensional array of islands. The short vertical distance of such layers of several nm generates an electronic coupling between adjacent islands and opens a way to tailor the wavelength of the emitted light. This multiple-stacking growth concept has been applied successfully to several systems of semiconductors [105,50]. The tuning of vertical and lateral correlation in QD superlattices by changes in the spacer thickness was demonstrated by Springholz et al. [106] especially for the PbSeTe system. This kind of self-organization is determined by the elastic anisotropy of the matrix material and by the growth orientation [107]. A first QD layer is covered with a GaAs capping layer, and subsequently about 2 ML of InAs are deposited. Due to surface diffusion, the first QD is covered with GaAs, with a second QD layer forming. In the case of ⟨001⟩ oriented substrates, the interaction between adjacent layers due to lattice strain variations induces a vertical alignment of islands.

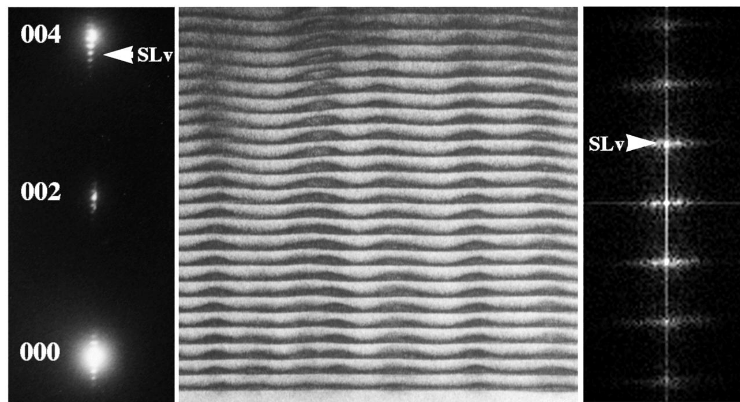

Fig. 15. Cross-section image of a multiple-stacked array of 25 InGaAs QD layers (dark islands, sample: Ioffe Institute, St. Petersburg) in a GaAs matrix (grey). The strong periodicity of the QD array is represented by subreflections in the SAD pattern (left) and the FFT diffractogram (right).

Fig. 15 shows a cross-section image of such a self-ordered assembly of InAs islands in GaAs. The micrograph demonstrates: i) the island size increases with the number of layers, ii) an improvement of the narrow size distribution, iii) a flattening of the growth surface by the GaAs spacer, especially for MBE

grown samples. The strong periodicity of the layers in the vertical direction is proven by the occurrence of satellite reflections near the main reflections in the SAD pattern (left). The horizontal periodicity of QDs is revealed by subreflections in the corresponding diffractogram (Fourier transformation, right). The first layer of InAs deposited is characterized by small flat islands (cf. schematic diagram of Fig. 9). Their homogeneously distributed strain fields cause the InAs islands to grow in size. For practical application in QD lasers, the active zone consists of stacks of two or three adjacent dot layers having an optimum light emitting characteristic. Other forms of stacking, e.g., are based on the idea to grow a first layer of small islands as seed layer for the following ones.

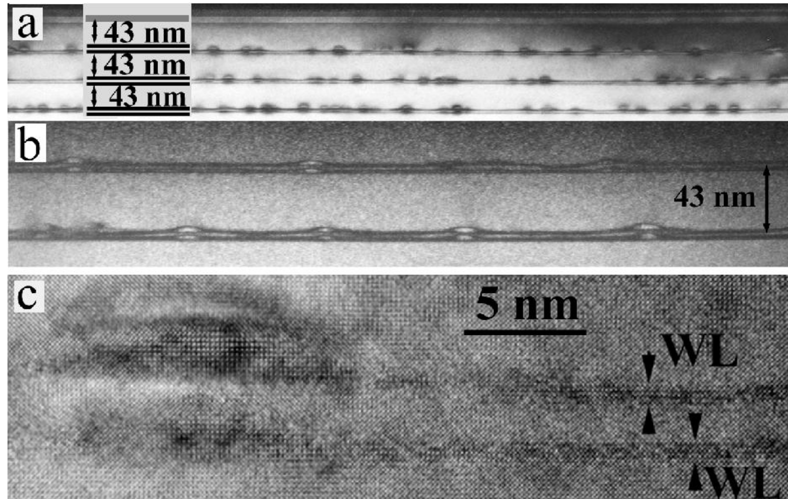

Fig. 16. Cross-section images of a heterostructure, which mainly consists of 3 double layers of InAs in GaAs grown by MOCVD (TU Berlin). Substrate orientation: ⟨001⟩. The bright-field image (a) shows mainly strain contrast caused by the dots and the wetting layer. A weak-beam dark-field image (b) allows to resolve the two dot layers having a distance of 3 nm. The bright contrast inside the dots corresponds to In, whereas the dark lines are caused by the lattice distortion.

Fig. 16 presents cross-section images of a structure, which consists of 3 layers separated by a 43 nm thick GaAs spacer. In the BF image (Fig. 16a) the dots are mainly visible by strain contrast. Due to the relatively large spacer of 43 nm a strain coupling between the layers does not exist and a correlation between the spots could not be observed. The dark-field weak-beam image (Fig. 16b) demonstrates that each layer itself consists of a stack of two adjacent sub-layers. According to the chosen growth parameters a strong coupling between the vertical islands was achieved, where the lower dots are of smaller size. In the HREM micrograph (Fig. 16c) the two adjacent flat

dots are visible. The lower one is not strong developed, however, initiated the formation of a larger dot having a diameter of about 14 nm and a height of about 3.5 nm. Also in this case the wetting layer close to the dots seems to be consumed during the island formation process. As mentioned above, similar extensive work has been carried out for the SiGe system. Also for this case of stacked structures growth parameters were elucidated [108–110]. In such stacked QD layers, excitons are not only localized at a single island, but could be at several adjacent ones. PL and CL measurements have shown that such arrays are characterized by a strong electronic coupling. This behaviour allows not only an emission (lasing) at room temperature, but a tailoring of the emitted wavelength due to a quantization in larger volumes. To improve the homogeneity of the QD size and density, further growth concepts have been developed, for instance, the island growth on vicinal surfaces, or the use of sub-MLs of InAs as seed layers for the subsequent conventional island growth (see Fig. 9e). A further possibility for attaining an emission for longer wavelength ($> 1.3\,\mu$m) has been demonstrated by generating laterally associated QD [51].

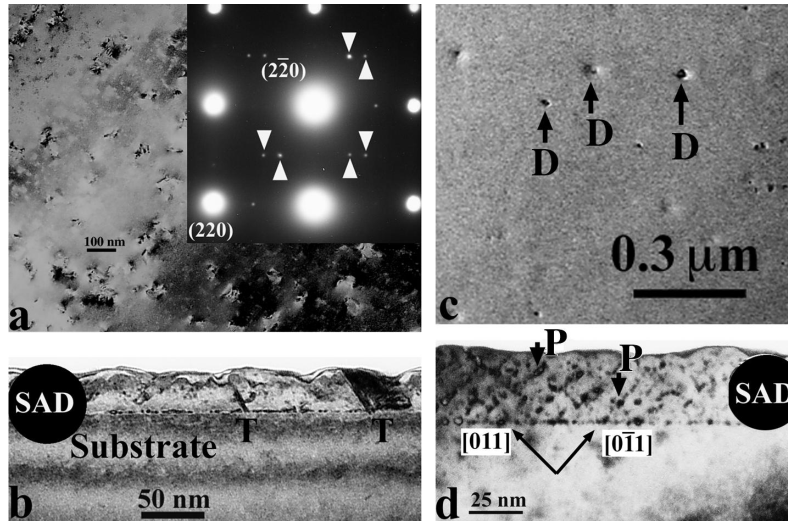

Fig. 17. Plan-view and cross-section TEM images of samples A (a,b) and sample B (c,d) respectively (samples: Ioffe Institute, St. Petersburg). In the [001] diffraction pattern from specimen A (see insert in (a)) extra reflections from precipitates are marked. c) Plan-view image of sample B. Defects marked as D are situated at the interface. (d) [100] cross-section image of sample B. (2×1) ordered InAs regions are marked as P.

3.3 QDs of InAs embedded in a silicon matrix

For future network communications optical circuits operating at wavelengths of 1.3 to 1.55 µm are interesting. The creation of Si-based emitters is complex due to the indirect band gap nature of Si. Many attempts to overcome the low radiative efficiency in Si have been made, such as porous silicon, Si-Ge quantum wells and quantum dots, and Si-Ge-C QDs and doping of Si with rare-earth impurities. These approaches have not found significant commercial applications up to now. Luminescence properties of indirect band gap material can be dramatically increased by insertions of direct narrow band gap media in an indirect matrix. The InAs/Si heteroepitaxial system could be assumed as a promising candidate for optoelectronic applications [4]. The InAs/Si heterostructure was grown by molecular beam epitaxy (MBE) on p-type Si(100) substrate. The nominal thickness of the deposited InAs was between 0.5 ML and 5 ML. Immediately after the InAs deposition, a Si cap layer was grown. After overgrowth with Si, these samples show an intense and broad luminescence line at a wavelength of about $1.3\,\mu m$ at $10K$ [111,52]. The corresponding plan-view and cross-section TEM images are presented in Fig. 17 for two samples A and B, prepared at different growth temperatures. Besides threading dislocations and other defects (marked by T, D), dark regions (P) are visible, which are analysed as InAs:Si inclusions [52].

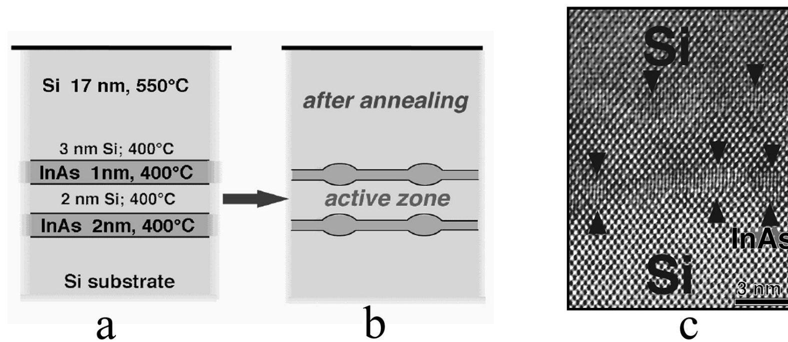

Fig. 18. (a) Growth schema of a InAs/Si heterostructure containing two InAs layers embedded in Si. (b) Due to kinetic processes during the layer growth small InAs inclusions are formed. (c) HREM lattice plane image of a cross-section sample including two InAs layers in a Si matrix.

A possible way to form stacked InAs nanoclusters in silicon is represented as an example in Fig. 18a→b. Two InAs layers of 2 nm and 1 nm thickness, respectively, were embedded by MBE in a Si matrix (a). After a special annealing procedure small coherent inclusions were formed as schematically shown in Fig. 18b. A surplus of InAs material was evaporated during this treatment. Corresponding PL spectra exhibited a luminescence band in the 1.3 µm re-

gion. HRTEM structure investigation of such samples [53,54] demonstrated that the coherent InAs nano-inclusions had a size of about 3 nm. In the cross-section image (Fig. 18c) the two layers of such clusters are marked by arrows. The observed PL luminescence was correlated to an indirect carrier transition of type-II in the small inclusions [54].

4 Conclusion and Outlook

The present overview serves as an introduction to the application of electron microscope methods to the investigation of nanostructures, especially to semiconductor quantum dots. In general, the morphology, size, strain fields and the density of QDs can be analyzed by TEM imaging. With the expected complexity of 3-dimensional QD structures, advanced TEM techniques are used (HREM, EFTEM), but also diffraction contrast TEM in combination with theoretical image interpretation. To yield data on the local lattice distortions one can apply combinations of image processing of HREM and conventional TEM micrographs with diffraction techniques, such as CBED. In addition, analytical methods (PL, CL) play an essential role in correlating the morphology and structure with the optoelectronic properties of semiconducting QD arrays.

Related to the different imaging techniques, the appearance of contrast features might be quite different: qualitatively one could distinct lattice plane images, black-white lobe DC, dot contrast with an oscillation behaviour as well as shifted HOLZ-lines in CBED pattern. In addition, there are contrasts due to the strain fields around a QD having symmetries influenced by the shape of the dots and the elastic properties of the matrix. Smaller dots show mainly loop-like contrasts prohibiding a unique analysis of the dot shape without additional contrast experiments or a priori information. As pointed out, the validity of TEM imaging techniques is partly restricted, e.g., due to the artificial strain changes in thin TEM specimens. It also has to be taken into consideration that TEM samples have a thickness below 50 nm and do not always include the whole dot structure or sufficient matrix material. This can cause some artifacts as wrong diameter/height ratios or artificial strain relaxations and renders more difficult the image interpretation. The difficulties may be partly avoided by using medium-voltage or high-voltage TEM, the actual developments towards more quantitative HREM, and enhanced interpretation techniques. For such improved quantitative analysis of TEM contrasts the experiments are interpreted using contrast simulations based on relaxed models and including the beam-object interaction as well as the imaging process itself. The TEM image formation can be simulated by means of the multi-slice algorithm evaluating the many-beam dynamical theory. A quantitative analysis demands carefully chosen imaging parameters and a suitably relaxed structure model. Geometric structure models and their relaxation behaviour can be studied, e.g., by molecular dynamics or molecular

static energy minimization. The improvement of computing capacity will allow the enhancement of such modeling and simulations discussed. In addition, always combinations of different methods have to be used supporting the TEM investigations for optimum results investigating island formation and their growth processes.

In summary, concerning materials science, the recent developments show the importance of quantum structures in semiconductor physics, and the increase of enhanced quantitative microscopy for structural analysis: investigations were started, which focused on several new material systems such as, e.g., silicon carbide, III-V nitrides, and nanoparticles in different matrices.

Acknowledgement

The authors would like to thank especially N.D. Zakharov from the MPI Halle for his contributions of TEM imaging of QD structures. We are also grateful to the following colleagues for their collaborations: F. Heinrichsdorff, R. Sellin, D. Bimberg from the Technische Universität Berlin; M. Grundmann, Universität Leipzig (in particular for providing strain-relaxed models of large dots); V. Ustinov, I. Soshnikov, G.E. Cirlin, and N.N. Ledentsov from the Ioffe Physical Technical Institute St. Petersburg/Russia; and A. Taurino from CNR Lecce/Italy.

References

1. D. Bimberg, M. Grundmann, N. N. Ledentsov: Quantum Dot Heterostructures, John Wiley & Sons., Chicester 1999
2. L. W. Wang, A. Zunger:‘Pseudopotential Theory of Nanometer Silicon Quantum Dots’, In: *Semiconductor Nanoclusters - Physical, Chemical, and Catalytic Aspects*, ed. by P. V. Kamat and D. Meisel, Elsevier Science 1997
3. F. Troiani, U. Hohenester, E. Molinari: Phys. Status Solidi (b) **224**, 849 (2001)
4. N.N. Ledentsov, V.M. Ustinov, A.Yu. Egorov, A.E. Zhukov, M.V. Maximov, I.G. Tabaradze, P.S. Kop’ev: Semiconductors **28**, 832 (1994)
5. N. Kirstaedter, N.N. Ledentsov, M. Grundmann, D. Bimberg, U. Richter, S.S. Ruvimov, P. Werner J. Heydenreich, V.M. Ustinov, M.V. Maximov, P.S. Kop’ev, Zh.I. Alferov: Electron. Lett. **30**, 1416 (1994)
6. O. Stier, M. Grundmann, D. Bimberg: Phys. Rev. B **59**, 5688 (1999)
7. S. Ruvimov, K. Scheerschmidt: Phys. Status Solidi (a) **150**, 471 (1995)
8. X. Z. Liao, J. Zou, X.F. Duan, D.J.H. Cockayne, R. Leon, C. Lobo: Phys. Rev B **58**, R4235 (1998)
9. K. Brunner, J. Zhu, G. Abstreiter, O. Kienzle, F. Ernst: Phys. Status Solidi (b) **224**, 531 (2001)
10. D. Bimberg, M. Grundmann, N.N. Ledentsov, M.H. Mao, Ch. Ribbat, R. Sellin, V.M. Ustinov, A.E. Zhukov. Zh.I. Alferov, J.A. Lott: Phys. Status Solidi (b) **224**, 787 (2001)
11. I.L. Krestnikov, N.N. Ledentsov, A. Hoffmann, D. Bimberg: Phys. Status Solidi (a) **183**, 207 (2001)
12. P. Kratzert, M. Rabe, F. Henneberger: Phys. Status Solidi (b) **224**, 179 (2001)

13. H. Lee, J. A. Johnson, M. Y. He, J. S. Speck, P.M. Petroff: Appl. Phys. Lett. **78**, 105 (2001)
14. A. Dunbar, M. Halsall, P. Dawson, U. Bangert, Y. Shiraki, M. Miura: Phys. Status Solidi (b) **224**, 257 (2001)
15. A. Dunbar, U. Bangert, P. Dawson, M. Halsall, Y. Shiraki, M. Miura, I. Berbezier, B.A. Joyce, J. Zhang: Phys. Status Solidi (b) **224**, 265 (2001)
16. A. Dunbar, M. Halsall, P. Dawson, U. Bangert, M. Miura, Y. Shiraki: Appl. Phys. Lett. **78**, 1658 (2001)
17. S. Schieker, O.G. Schmidt, K. Eberl, N.Y. Jin-Phillipp, F. Phillipp: Appl. Phys. Lett. **72**, 3344 (1998)
18. S. Oktyabrsky, V. Tokranov, M. Yakimov, A. Katsnelson, K. Dovidenko: Mat. Res. Soc. Symp. Proc. **642**, J3.30.1 (2001)
19. N.N. Ledentsov, D. Litvinov, A. Rosenauer, D. Gerthsen, I.P. Soshnikov, V.A. Shchukin, V.M. Ustinov, A.Yu. Egorov, A.E. Zukov, V.A. Volodin, M.D. Efremov, V.V. Preobrazhenskii, B.P. Semyagin, D. Bimberg, Z.I. Alferov: J. Electron. Mater. **30**, 463 (2001)
20. M. de Giorgi, A. Passaseo, R. Rinaldi, T. Johal, R. Cingolani, A. Taurino, M. Catalano, P. Crozier: Phys. Status Solidi (b) **224**, 17 (2001)
21. Q. Zhang: Appl. Phys. Lett. **78**, 3830 (2001)
22. A. Rosenauer, D. Gerthsen: Ultramicroscopy **76**, 49 (1999)
23. A. Rosenauer, D. van Dyck, D. Gerthsen, M. Arzberger, G. Böhm, G. Abstreiter: Phys. Status Solidi (b) **224**, 213 (2001)
24. T.W. Kim, D.U. Lee, D.C. Choo, H.J. Kim, H.S. Lee, J.Y. Lee, M.D. Kim, S.H. Park, H.L. Park: Solid State Commun. **1180**, 465 (2001)
25. J.P. McCaffrey, M.D. Robertson, Ph. Poole, Z.R. Wasilewski, B. Riel, R. Williams, S. Fafard: Mat. Res. Soc. Symp. Proc. **642**, J8.5.1 (2001)
26. E. Kurtz, M. Schmidt, M. Baldauf, D. Litvinov, D. Gerthsen, H. Kalt, C. Klingshirn: Phys. Status Solidi (b) **224**, 185 (2001)
27. D. Litvinov, D. Gerthsen, A. Rosenauer, H. Preis, E. Kurtz, C. Klingshirn: Phys. Status Solidi (b) **224**, 143 (2001)
28. D. Litvinov, A. Rosenauer, D. Gerthsen, H. Preis, S. Bauer, E. Kurtz: J. Appl. Phys. **89**, 4150 (2001)
29. Y.-T. Moon, D.J. Kim, K.M. Song, C.J. Choi, S.H. Han, T.Y. Seong, S.J. Park: J. Appl. Phys., **89**, 6514 (2001)
30. Z. Liliental-Weber, M. Benamara, J. Washburn, J.Z. Domagala, J. Bak-Misiuk, E.L. Piner, J.C. Roberts, S.M. Bedair: J. Electron. Mater. **30**, 439 (2001)
31. N.Y. Jin-Phillipp, F. Phillipp: J. Appl. Phys. **88**, 710 (2000)
32. B.H. Choi, C.M. Park, S.H. Song, M.H. Son, S.W. Hwang, D. Ahn, E.K. Kim: Appl. Phys. Lett. **78**, 1403 (2001)
33. T. Baron, F. Martin, P. Mur, C. Wyon, M. Dupuy, C. Busseret, A. Souifi, G. Guillot: Mat. Res. Soc. Symp. Proc. **571**, 37 (2000)
34. F. Yun, B.J. Hinds, S. Hatatani, S. Oda, Q.X. Zhao, M. Willander: Thin Solid Films **375**, 137 (2000)
35. F.M. Ross, J. Tersoff, R.M. Tromp: Phys. Rev. Lett. **80**, 984 (1998)
36. F. M. Ross, R.M. Tromp, M.C. Reuter: Science **286**, 1931 (1999)
37. R.Leon, S. Marcenkevicius, X.Z. Liao, J. Zou, D.J.H. Cockayne, S. Fafard: Phys. Rev. B **58**, R8517 (1999)
38. J. Zuo, X.Z. Liao, D.J.H. Cockayne, R. Leon: Phys. Rev. B **59**, 12279 (1999)
39. X. Z. Liao, J. Zou, D.J.H. Cockayne, R. Leon, C. Lobo: Phys. Rev. Lett. **82**, 5148 (1999)

40. Y. Androussi, T. Benabbas, A. Levebvre: Philos. Mag. Lett. **79**, 201 (1999)
41. K. Scheerschmidt, D. Conrad, H. Kirmse, R. Schneider, W. Neumann: Ultramicroscopy **81**, 289 (2000)
42. I. Daruka, A.-L. Barabasi, S.J. Zhou, T.C. Germann, P.S. Lomdahl, A.R. Bishop: Phys. Rev. B **60**, R2150 (1999)
43. A.D. Andreev, J.R. Downes, D.A. Faux, E.P. O'Reilly: J. Appl. Phys. **86**, 297 (1999)
44. T. Benabbas, P. Francois, Y Androussi, A. Lefebvre: J. Appl. Phys. **80**, 2763 (1996)
45. G.D. Lian, J. Yuan, L.M. Brown, G.H. Kim, D.A. Ritchie: Appl. Phys. Lett., **73**, 49 (1998)
46. S. Rouvimov, Z. Liliental-Weber, W. Swider, J. Washburn, E.R. Weber, A. Sasaki, A. Wakahara, Y. Furkawa, T. Abe, S. Noda: J. Electron. Mater. **27**, 427 (1998)
47. S. Ruvimov, P. Werner, K. Scheerschmidt, U. Richter, J. Heydenreich, U. Gösele, N.N. Ledentsov, M. Grundmann, D. Bimberg, V.M. Ustinov, A.Yu. Egorov, P.S. Kop'ev, Zh.I. Alferov: Phys. Rev. B **51**, 14766 (1995)
48. P. Werner, K. Scheerschmidt, N.D. Zacharov, R. Hillebrand, M. Grundmann, R. Schneider: Cryst. Res. Technol. **35**, 759 (2000)
49. Y. Wakayama, G. Gerth, P. Werner, U. Gösele: Appl. Phys. Lett. **77**, 2328 (2000)
50. F. Heinrichsdorff, M.H. Mao, N. Kirstaedter, A. Krost, D. Bimberg, A. Kosogov, P. Werner: Appl. Phys. Lett. **71**, 22 (1997)
51. M.V. Maximov., A.F. Tsatsulnikov, B.V. Volovik, D.A. Bedarev, A.Yu. Egorov, A.E. Zhukov, A.R. Kovsh, N.A. Bert, V.M. Ustinov, Zh.I. Alferov, N.N. Ledentsov, D. Bimberg, I.P. Soshnikov, P. Werner: Appl. Phys. Lett. **75**, 2347 (1999)
52. N.D. Zakharov, P. Werner, U. Gösele, R. Heitz, D. Bimberg, N.N. Ledentsov, V.M. Ustinov: Appl. Phys. Lett. **76**, 2677 (2000)
53. N.D. Zakharov, P. Werner, U. Gösele, R. Heitz, D. Bimberg, N.N. Ledentsov, V.M. Ustinov, B.V. Volovik, Zh.I. Alferov, N.K. Polyakov, V.N. Petrov, V.A. Egorov, G.E. Cirlin: Symposium Mat. Res. Soc. Symp. Proc., Spring Meeting 1999, in press.
54. R. Heitz, N.N. Ledentsov, D. Bimberg, A.Yu. Egorov, M.V. Maximov, V.M. Ustinov, A.E. Zhukov, Zh.I. Alferov, G.E. Cirlin, I.P. Soshnikov, N.D. Zakharov, P. Werner, U. Gösele: Appl. Phys. Lett. **74**, 1701 (1999)
55. N.D. Zakharov, R. Sellin, M. Grundmann, D. Bimberg, P. Werner: Appl. Phys. Lett., (2001) in press.
56. M. Grundmann, O. Stier, S. Bognar, C. Ribbat, F. Heinrichsdorff, D. Bimberg: Phys. Status Solidi (a) **178**, 255 (2000)
57. M. Califano, P. Harrison: Mat. Res. Soc. Symp. Proc. **640**, J1.4.1 (2001)
58. H.T. Johnson, V. Nguyen, A.F. Bower: Mat. Res. Soc. Symp. Proc. **642**, J1.9.1 (2001)
59. A. Zunger: Phys. Status Solidi (b) **224**, 727 (2001)
60. P.N. Keating: Phys. Rev. **145**, 637 (1966)
61. Y. Kikuchi, H. Sugii, K. Shintani: J. Appl. Phys. **89**, 1191 (2001)
62. H. Balamane, T. Halicioglu, W.A. Tiller: Phys. Rev. B **46**, 2250 (1992)
63. J. Tersoff: Phys. Rev. B **38**, 9902 (1989)
64. J. Tersoff: Phys. Rev. B **39**, 5566 (1989)

65. D. Conrad, K. Scheerschmidt: Phys. Rev. B **58**, 4538 (1998)
66. D.G. Pettifor, I.I. Oleinik: Phys. Rev. B **59**, 8487 (1999)
67. D. Conrad, K. Scheerschmidt, U. Gösele: Appl. Phys. Lett. **77**, 49 (2000)
68. CERIUS program package. Molecular Simulations Inc., San Diego.
69. H.H. Kang: Mater. Sci. Eng. B **80**, 104 (2001)
70. J.W. Edington: Practical Electron Microscopy in Material Science, The MacMillan Press, London 1977
71. K.P. Chick, M. Wilkens, M. Rühle: Phys. Status Solidi **23**, 111 (1967)
72. D. Lepski: Phys. Status Solidi (a) **23**, 543 (1974)
73. K. Scheerschmidt, U. Gleichmann: 'Lattice Defect Imaging by Diffraction Contrast'. In: *H. Bethge, J. Heydenreich (Eds.), Electron Microscopy in Solid State Physics, Elsevier Materials Science Monographs 40*, Amsterdam 1987, pp.289–324.
74. A.F. Ashby, L.M. Brown: Phil. Mag. **8**, 1649 (1963)
75. K.G. McIntyre, L.M.J. Brown: Phys. Radium **27**, C3 (1966)
76. C.P. Liu, P.D. Miller, W.L. Henstrom, J.M. Gibson: J. Microsc. **199**, 130 (2000)
77. D. Lepski: Phys. Status Solidi (a) **66**, 479 (1980)
78. S. Christiansen, M. Albrecht, H. P. Strunk, H. J. Maier: Appl. Phys. Lett. **64**, 3617 (1994)
79. P. A. Stadelmann: Ultramicroscopy **21**, 131 (1987)
80. H. Kirmse, W. Neumann, T. Wiebach, R. Köhler, K. Scheerschmidt, D. Conrad: Mater. Sci. Eng. B **69**, 361 (2000)
81. D. van Dyck, J. Microsc. **190**, 190 (1998)
82. G. Möbus, R. Schweinfest, T. Gemming, T. Wagner, M. Rühle: J. Microsc. **190**, 109 (1998)
83. C. Kisielowski, P. Schwander, F.H. Baumann, M. Seibt, Y. Kim, A. Ourmazd: Ultramicroscopy **58**, 131 (1995)
84. P. Schwander, W.D. Rau, A. Ourmazd: J. Microsc. **190**, 171 (1998)
85. J. Stenkamp, W. Jäger: Inst. Phys. Conf. Ser. **134**, 15 (1993)
86. A. Ourmazd, F.H. Baumann, M. Bode, Y. Kim: Ultramicroscopy **34**, 237 (1990)
87. H. Seitz, M. Seibt, F.H. Baumann, K. Ahlborn, W. Schröter: Phys. Status Solidi (a) **150**, 625 (1995)
88. R. Bierwolf, M. Hohenstein, F. Phillipp, O. Brandt, G.E. Crook, K. Ploog: Ultramicroscopy **49**, 273 (1993)
89. A. Rosenauer, D. Gerthsen: Adv. Imaging and Electron Phys. **107**, 121 (1999)
90. D. Stenkamp, H.P. Strunk: Appl. Phys. A **62**, 369 (1996)
91. M.J. Hytch, W.M. Stobbs: Ultramicroscopy **53**, 63 (1994)
92. R. Hillebrand: J. Microsc. **190**, 61 (1998)
93. R. Hillebrand, H. Kirschner, P. Werner, U. Gösele: Phys. Status Solidi (b) **222**, 185 (2000)
94. A. Rosenauer, U. Fischer, D. Gerthsen, A. Förster: Ultramicroscopy **72**, 121 (1998)
95. P.A. Midgley, J. Barnard, D. Cherns: 'The use of electron holography for composition profiling of semiconductor heterostructures'. In: *Microscopy of Semiconducting Materials 1997, Proc. of the Royal Microsc. Soc., IOP Publishing 1997*, ed. by A.G. Cullis and J.L. Hutchison, Bristol, UK, 1997, pp.75–78.
96. G. Ade: 'Determination of the geometrical dimensions of quantum dots and measurement of lattice distortions'. In: *Proc. 3rd Seminar Quantitative Microscopy, Phys-Tech Bundesanstalt, Braunschweig and Berlin 1998*, Germany, pp. 82–88.

97. K.H. Schmidt G. Medeiros-Ribeiro, M. Cheng, P.M. Petroff: Mater. Res. Soc. Symp. Proc. **452**, Pittsburgh 1997, pp. 275
98. C. Teichert, M.G. Lagally, L.J. Peticolas, J.C. Bean, J. Tersoff: Phys. Rev. B **53**, 16334 (1996)
99. C. Teichert, C. Hofer, K. Lyutovich, M. Bauer, E. Kasper: Thin Solid Films **380**, 25 (2000)
100. S. Christiansen, M. Albrecht, H.P. Strunk, H.J. Maier: Appl. Phys. Lett. **64**, 3617 (1994) Comput. Mater. Sci. **7** 213 (1996)
101. M. Goryll, L. Vescan, K. Schmidt, S. Mesters, H. Lth, K. Szot: Appl. Phys. Lett. **71**, 410 (1997)
102. C.-P. Liu, P.D. Miller, W.L. Nenstrom, J.M. Gibson: J. Microsc. **199**, 130 (2000)
103. R. Schneider, H. Kirmse, W. Neumann, F. Heinrichsdorff, D. Bimberg: Inst. Phys. Conf. Ser. **164**, 31 (1999)
104. H. Eisele, O. Flebbe, T. Kalka, C. Preinesberger, F. Heinrichsdorff, A. Krost, D. Bimberg, M. Daehne-Prietsch: Appl. Phys. Lett. **75**, 106 (1999)
105. J. Tersoff, Ch. Teichert, M.G. Lagalli: Phys. Rev. Lett. **76**, 1675 (1996)
106. G. Springholz, M. Pinczolits, P. Mayer, V. Holy, G. Bauer, H.H. Kang: Phys. Rev. Lett. **84**, 4669 (2000)
107. V. Holy, G. Springholz, M. Pinczolits, G. Bauer: Phys. Rev. Lett. **83**, 356 (1999)
108. O.G. Schmidt, O. Kienzle, Y. Hao, K. Eberl, F. Ernst: Appl. Phys. Lett. **73**, 659 (1998)
109. O.G. Schmidt, O. Kienzle, Y. Hao, K. Eberl, F. Ernst: Appl. Phys. Lett. **74**, 1272 (1999)
110. G. Abstreiter, P. Schittenhelm, C. Engel, E. Silveira, A. Zrenner, D. Meertens, W. Jäger: Semicond. Sci. Technol. **11**, 1521 (1996)
111. G.E. Cirlin, V.G. Dubrovskii, V.N. Petrov, N.K. Polyakov, N.P. Korneeva, V.N. Demidov, A.O. Golubok, S.A. Masalov, D.V. Kurochkin, O.M. Gorbenko, N.I. Komyak, V.M. Ustinov, A.Yu. Egorov, A.R. Kovsh, M.V. Maximov, A.F. Tsatsul'nikov, B.V. Volovik, A.E. Zhukov, P.S. Kop'ev, Zh.I. Alferov, N.N. Ledentsov, M. Grundmann, D. Bimberg: Semicond. Science and Technol. **13**, 1262 (1998)